COMMUNICATION

Check for updates

Active faceted nanoporous ruthenium for electrocatalytic hydrogen evolution†

Abdillah Sani Bin Mohd Najib, [abc] Muhammad Iqbal, [b]
Mohamed Barakat Zakaria, [d] Shusaku Shoji,[e] Yohei Cho,[e] Xiaobo Peng, [b]
Shigenori Ueda, [fg] Ayako Hashimoto, [g] Takeshi Fujita, [h] Masahiro Miyauchi, [e]
Yusuke Yamauchi [*di] and Hideki Abe [*ab]

Nanoporous ruthenium (np-Ru) comprising reaction active facets is synthesized from a ruthenium–cerium (Ru_2Ce) alloy precursor. Spontaneous nanophase separation of Ru_2Ce in an oxidative atmosphere results in a lamellar nanocomposite consisting of Ru metal and cerium oxide (CeO_2). Selective leaching of the Ru–CeO_2 nanocomposite in sulfuric acid yields np-Ru with a high surface area of 48 m^2 g^{-1}, predominantly surrounded by reaction active $\{10\bar{1}0\}$ facets. Active-faceted np-Ru efficiently catalyzed the hydrogen evolution reaction (HER) in acidic media at an overpotential of +74 mV *vs.* the reversible hydrogen electrode, which is 20 mV lower than that for carbon-supported Ru (Ru/C) and rather close to +58 mV for state-of-the-art Pt/C. Np–Ru has great potential in broad applications such as hydrogen battery electrodes because of its low HER overpotential and scalable synthetic protocol.

Nanoporous materials are one of the confocal subjects of broad research on catalysts, absorbates and sensors due to their large surface area as a stage for different molecular events.[1,2] Metallic nanoporous materials, *i.e.*, nanoporous metals, are of particular and growing interest because of their high thermal/electric conductivity, magnetic , and plasmonic properties.[3–5] There are a number of successful attempts to tailor the nanopores in size, dispersity and connectivity, using templates such as block copolymers, liquid crystals and/or mesoporous silica.[6–11] The nanoporous metals synthesized in such bottom-up approaches are inherently an aggregate of individual clusters deposited to the template surface. Different approaches such as dealloying of prepared alloy precursors may yield more favorable nanoporous metals for electrocatalytic applications because of their continuously connected network structure.[12–17] The so far developed dealloying methods can, however, hardly tailor the surface atomic arrangement of nanoporous metals: dealloyed metals are usually surrounded by randomly developed facets, some of which can inhibit targeted surface reactions.[18]

Herein, we propose another versatile method to synthesize facet-tailored nanoporous metals, utilizing a spontaneous nanophase-separation phenomenon of alloy precursors. An alloy precursor consisting of the target metal and an oxyphilic metal counterpart is subjected to an oxidative atmosphere to promote internal oxygen diffusion. Selective oxidation of the counterpart metal results in a spatially ordered metal-oxide nanocomposite. As the result of a strong metal–oxygen interaction at the epitaxial interface, the metal phase is allowed to develop energetically unfavorable crystal planes. The oxide counterpart is finally leached out in solvent to yield the targeted nanoporous metal that is surrounded by reaction active facets.

Precious-Group Metals (PGMs) especially platinum (Pt) serve as prominent catalysts for different chemical reactions.[19–22] Electrolytic hydrogen (H_2) evolution from aqueous solution (Hydrogen Evolution Reaction: HER) can potentially produce CO_2-free H_2, yet is precluded from broad use due to the lack of reaction active and economically sound electrocatalysts.[23] It is highly desirable to materialize nanoporous ruthenium (np-Ru) as an efficient alternative to the state-of-the-art, expensive Pt electrocatalysts for the HER (Pt: 30 $ g^{-1}; Ru: 8 $ g^{-1} – Johnson

aGraduate School of Science and Technology, Saitama University, Shimo-Okubo 255, Saitama 338-8570, Japan. E-mail: BE.Hideki@Anims.go.jp

bNational Institute for Materials Science, 1-1 Namiki, Tsukuba, Ibaraki 305-0044, Japan

cSchool of Mechanical engineering, Faculty of engineering, Universiti Teknologi Malaysia, Skudai, Johor Bahru, 81310, Malaysia

dAustralian Institute for Bioengineering and Nanotechnology (AIBN) and School of Chemical Engineering, The University of Queensland, Brisbane, QLD, 4072, Australia. E-mail: y.yamauchi@uq.edu.au

eDepartment of Materials Science and Engineering, School of Materials and Chemical Technology, Tokyo Institute of Technology, Ookayama 2-12-1, Meguro-ku, Tokyo 152-8552, Japan

fSynchrotron X-ray Station at SPring-8, National Institute for Materials Science, 1-1-1 Kouto, Sayo, Hyogo, 679-5148, Japan

gNational Institute for Materials Science, 1-2-1 Sengen, Tsukuba, Ibaraki, 305-0047, Japan

hSchool of Environmental Science and Engineering, Kochi University of Technology, 185 Miyanokuchi, Tosayamada, Kami City, Kochi 782-8502, Japan

iDepartment of Plant & Environmental New Resources, Kyung Hee University, 1732 Deogyeong-daero, Giheung-gu, Yongin-si, Gyeonggi-do 446-701, South Korea

† Electronic supplementary information (ESI) available. See DOI: 10.1039/d0ta04223d

19788 | *J. Mater. Chem. A*, 2020, 8, 19788–19792

This journal is © The Royal Society of Chemistry 2020

Matthey). However, to date, most of the attempts to synthesize np-Ru by conventional dealloying[24,25] and organometallic decomposition[26] methods resulted in the emergence of random facets which diminished the catalytic performance: the {10$\bar{1}$0} facets of hexagonal Ru are theoretically demonstrated as most HER active, but less readily developed than any of the other energetically favorable facets.[27]

To demonstrate the priority of the proposed approach for nanoporous metals, we have successfully synthesized np-Ru from a precursor alloy consisting of Ru and a highly oxyphilic metal counterpart, cerium (Ce) (Fig. 1).[28] A Ru$_2$Ce alloy was first subjected to an oxidative environment to promote nanophase separation into a Ru–CeO$_2$ nanocomposite. The Ru and CeO$_2$ phases were ordered in a nanometer-thick ($\sim$5 nm) lamellar structure because oxygen atoms diffuse throughout the precursor so as to extend an epitaxial interface of the CeO$_2${110} and Ru {10$\bar{1}$0} planes. Selective leaching of the CeO$_2$ phase in sulfuric acid (H$_2$SO$_4$) finally yielded phase-pure, highly crystalline np-Ru that was predominantly surrounded by {10$\bar{1}$0} facets. The active faceted np-Ru efficiently promoted the HER in acidic media at a lower overpotential than carbon-supported Ru (Ru/C) with a higher turn-over frequency (TOF) at +100 mV vs. the reversible hydrogen electrode (RHE) compared to previously reported metallic np-Ru (Fig. S1 and S2†).[26]

The Ru$_2$Ce alloy precursor was prepared by melting Ru and Ce metal ingots using an arc torch in a pure Ar atmosphere. The precursor alloy was then powdered with a mortar, sieved to 50–60 μm in size and heated in a mixture of carbon monoxide (CO), oxygen and argon gas (CO : O$_2$: Ar = 1 : 1 : 98 in volumetric ratio; flow rate = 60 cm^3 s^{-1}) at 600 °C for 12 hours. Powder X-ray diffractometry (pXRD) demonstrated that the reflections from the Ru$_2$Ce precursor were fully substituted by those from Ru metal and CeO$_2$ after the atmosphere treatment (Fig. S3†). Cross-sectional scanning transmission electron microscopy (STEM) observation further showed that the atmosphere-treated Ru$_2$Ce alloy was converted into a Ru–CeO$_2$ nanocomposite consisting of a highly ordered lamellar structure with a spatial period of 5 nm (Fig. 2a, b; see Fig. S4†). The bright and dark contrasted areas in Fig. 2a correspond to the metal Ru and CeO$_2$ phases, respectively, as supported by compositional mapping (Fig. 2b; see Fig. S5† for details).

Fig. 2 (a) Cross-sectional annular-dark field (ADF) scanning transmission electron microscopy (STEM) image and (b) compositional mapping image of a nanophase-separated Ru–CeO$_2$ composite obtained from precursor Ru$_2$Ce via atmosphere treatment. The red and dark green stripes correspond to the Ru and CeO$_2$ phases, respectively. (c) High-resolution transmission electron microscopy (TEM) image of the Ru–CeO$_2$ interface. (d) A schematic model for the epitaxial relationship between the Ru{10$\bar{1}$0} and CeO$_2${110} planes. The red, blue and green circles correspond to the Ru, Ce and O atoms, respectively.

The Ru phase was developed such that the Ru{10$\bar{1}$0} and CeO$_2${110} planes were oriented with an epitaxial relationship (Fig. 2c; S3 and S7†). The interatomic distance of oxygen on the CeO$_2$ (110) planes along the [100] axis, 2.7 Å, matches with the interatomic distance of Ru on the Ru (10$\bar{1}$0) planes along the [11$\bar{2}$0] axis, 2.7 Å (Fig. S8†).[29] This lattice matching may minimize the interfacial energy between the metal and oxide phases to favor the epitaxial Ru{10$\bar{1}$0}/CeO$_2${110} interface. Note that in the pXRD spectra, the {10$\bar{1}$0} reflections were clearly visible for np-Ru due to the preferred growth of the {10$\bar{1}$0} facets, while much weak reflections were recognized for directly dealloyed Ru$_2$Ce having polycrystalline nature (Fig. S3†).

Subsequent selective leaching of CeO$_2$ from the Ru–CeO$_2$ nanocomposite (Fig. 3a) in H$_2$SO$_4$ solution resulted in the targeted, faceted np-Ru (Fig. 3b). The CeO$_2$ phase was completely removed as evidenced by pXRD and hard X-ray photoemission spectroscopy (HAXPES) (Fig. S3 and S9†). The Ru{10$\bar{1}$0} facets, which were extended via the formation of the Ru{1010}/Ce{110} interface in the nanophase separation of the precursor alloy, became fully exposed to the environment after the elimination of the CeO$_2$ matrix (Fig. 3c and d, see Fig. S10† for FFT analysis). The specific surface area of np-Ru was quantified by BET (Brunauer–Emmett–Teller) surface area measurements as 48 m^2 g^{-1}. The nitrogen (N$_2$) adsorption–desorption isotherm demonstrated a hysteresis trend, showing that np-Ru consisted of slit-shaped and/or lamellar pores, as expected from the transmission electron microscopy (TEM) observations (Fig. S11†).
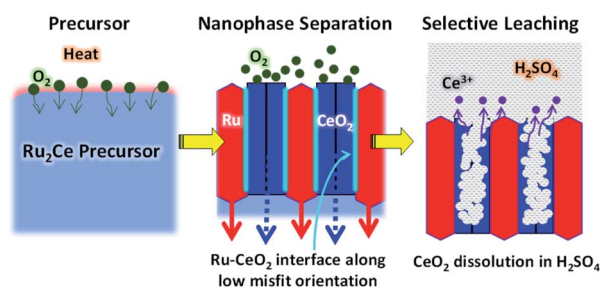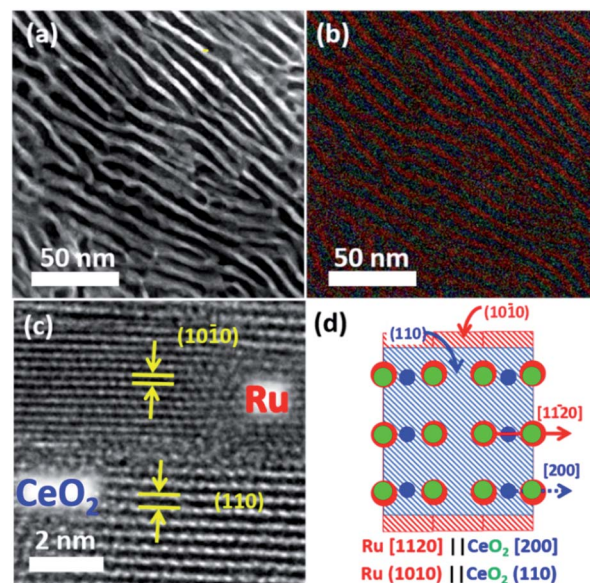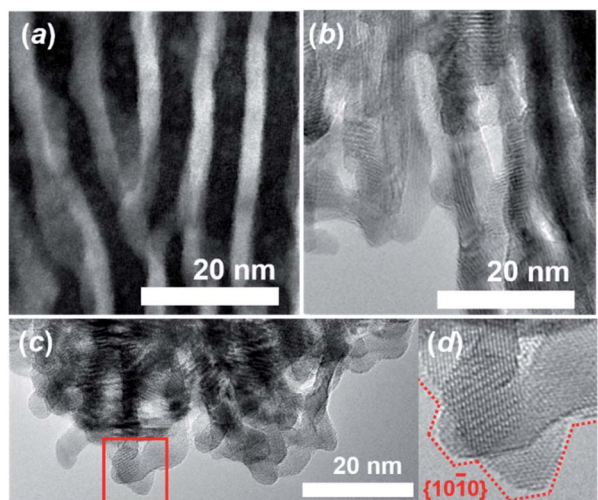

Fig. 1 Synthetic protocol for active faceted np-Ru. Heating the Ru$_2$Ce alloy precursor in an oxidative atmosphere results in a nanophase-separated metal-oxide composite having an extended Ru{10$\bar{1}$0}/CeO$_2${110} epitaxial interface. The nanocomposite is finally leached in sulfuric acid to selectively dissolve CeO$_2$, yielding active faceted np-Ru.

This journal is © The Royal Society of Chemistry 2020

J. Mater. Chem. A, 2020, 8, 19788–19792 | 19789

Fig. 3 (a) Cross-sectional ADF STEM image of a nanophase-separated Ru–CeO$_2$ nanocomposite (bright: Ru; dark: CeO$_2$) and (b) a bright-field transmission electron microscopy (TEM) image of active faceted np-Ru obtained via a selective leaching of the Ru–CeO$_2$ nanocomposite (dark: Ru; bright: vacuum). (c) Bright-field TEM images of active faceted np-Ru. The atomic fringes in (d) correspond to the Ru {10$\bar{1}$0} planes.

Cyclic Voltammetry (CV) was conducted in 0.5 M H$_2$SO$_4$ solution using a rotating glassy-carbon disk electrode to identify the preferential facets of np-Ru. Fig. 4a presents the CV profiles for np-Ru and carbon-supported Ru (Ru/C; loading weight: 5%). Ru/C showed a typical CV profile for polycrystalline Ru with no preferential facets. By contrast, np-Ru showed a CV profile having distinct peaks at +0.30 V and +0.52 V vs. RHE, corresponding to the electrochemical oxidation of chemisorbed
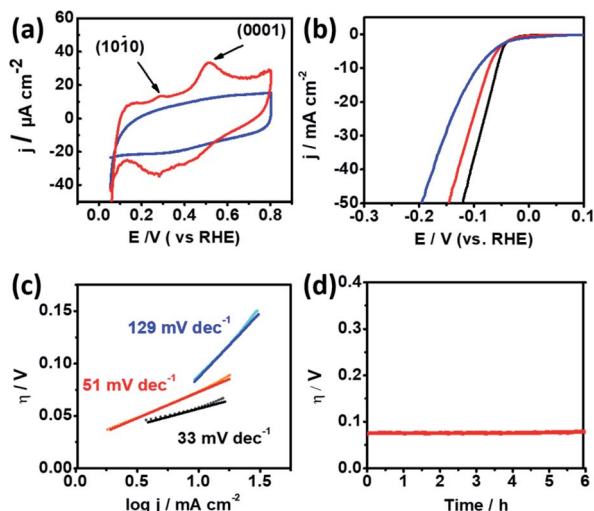

Fig. 4 (a) Cyclic Voltammetry (CV) profiles for np-Ru (red) and Ru/C (blue), and (b) Linear Sweep Voltammetry (LSV) profiles and the corresponding (c) Tafel plots for np-Ru (red), Ru/C (blue) and Pt black (black). The corresponding Tafel slopes are shown in the inset. (d) Chronogalvanometry profile for np-Ru (red) acquired at a HER current density of 10 mV s^{-1}. All the experiments were conducted in 0.5 M H$_2$SO$_4$ solution using platinum wire as the counter electrode.

hydrogen atoms over the {10$\bar{1}$0} and {0001} facets, respectively.[30] As expected from the TEM characterization (Fig. 2d–f and S7†), np-Ru was predominantly surrounded by the {10$\bar{1}$0} and {0001} facets.

Linear Sweep Voltammetry (LSV) was performed in 0.5 M H$_2$SO$_4$ in a potential range from +100 mV to −400 mV vs. RHE to evaluate the HER performance of the faceted np-Ru catalyst (by considering overpotential at current density, j of 10 mA cm^{-2}).[26,31,32] As a comparison, Ru/C and Pt black were also tested under the same conditions. The polarization curves resulting from LSV demonstrated that np-Ru had an overpotential of −74 mV. This value was significantly low compared to the overpotential of −94 mV for Ru/C, and rather close to that for the state-of-the-art Pt/C, −58 mV (Fig. 4b).

We performed LSV using a graphite rod as the counter electrode to avoid possible contamination by redeposition of Pt (Fig. S12†).[33] Another control LSV experiment was conducted in a perchloric acid (HClO$_4$) electrolyte to avoid possible contamination by adsorption of sulfuric anions (SO$_4^{2-}$) (Fig. S13†). The np-Ru catalyst was superior to Ru/C in the both cases in terms of higher onset potentials. np-Ru also showed higher HER mass activity than a non-supported metal Ru catalyst (Fig. S14, see the ESI† for the synthetic details of metal Ru). The electrochemical surface areas (ECSAs) for np-Ru and Ru/C were determined to be 39.60 and 73.87 m^2 g^{-1}, respectively, by measuring the double-layer capacitance in the electrolyte solution (Fig. S15, see the ESI† for experimental details).[34–38] The current density normalized to the ECSA finally supported that np-Ru was superior to Ru/C in HER activity (Fig. S16†).

Furthermore, the Tafel slopes derived from LSV for np-Ru, +51 mV dec^{-1}, was much lower than that for Ru/C, +129 mV dec^{-1}, and again closer to that of Pt black, +33 mV dec^{-1}. The np-Ru catalyst promoted the HER not only at a lower overpotential but also kinetically fast compared to Ru/C (Fig. 4c). In addition, the exchange current density at zero overpotential (J_0) from the Tafel extrapolation method for np-Ru, PtB, and Ru/C was estimated to be 22.67 mA cm^{-2}, 17.25 mA cm^{-2}, and 6.638 mA cm^{-2}, respectively (Fig. S17†). The np-Ru catalyst exhibited a higher exchange current density than Ru/C, indicating that the np-Ru surface had a so low energy barrier that charge is readily transported between the electrolyte and the catalyst surface.

It is acknowledged that there are three rate-determining steps associated with the HER in acidic media, resulting in different Tafel slopes: reduction of hydronium ions, H$_3$O$^+$ to H adatoms, H$_{ads}$ (Volmer reaction: H$_3$O$^+$ + e$^-$ + M → H$_{ads}$ + H$_2$O; A = 120 mV dec^{-1}), electrochemical desorption (Heyrovsky reaction: H$_{ads}$ + H$_3$O$^+$ + e$^-$ → H$_2$ + H$_2$O + M; A = 40 mV dec^{-1}) and pairing of H$_{ads}$ to form molecular H$_2$ (Tafel reaction: 2H$_{ads}$ → H$_2$ + 2M; A = 30 mV dec^{-1}) where M corresponds to the surface empty site.[39,40]

Based on the calculated Tafel slopes, the rate-determining step for Ru/C is assigned to the Volmer reaction in which H$_3$O$^+$ reduction to H$_{ads}$ was relatively slow. By contrast, the np-Ru catalyst promotes the HER predominantly via the Volmer–Heyrovsky reaction, where H$_{ads}$ was readily available to be desorbed via electrochemical pathways. As theoretically

19790 | J. Mater. Chem. A, 2020, 8, 19788–19792

This journal is © The Royal Society of Chemistry 2020

demonstrated by Li *et al.*, the Ru {10$\bar{1}$0} and {0001} facets moderately adsorb H_{ads} compared to the other facets including {11$\bar{2}$0}.[27] The moderately adsorbed H_{ads} onto the {10$\bar{1}$0} facets can serve as an active intermediate for the other reactions, *i.e.*, hydronium ions to molecular H_2 (Heyrovsky) as for np-Ru, whereas too strongly adsorbed H_{ads} depletes the surface empty site, M, slowing down further generation of active H_{ads} (Volmer) as for Ru/C.[41] Electrochemical impedance spectroscopy demonstrated a small arc diameter for np-Ru compared to that for Ru/C, showing that np-Ru had a lower resistance at the electrode/electrolyte interface (Fig. S18†). The low electrode/electrolyte resistance is associated with better diffusion of hydrogen, electrolyte, and intermediate species.[34] The improved HER catalytic activity of np-Ru is thus partly attributed to the lowered charge-transfer resistance at the catalyst/electrode interface.

The catalyst stability of np-Ru was evaluated by chronogalvanometry in 0.5 M H_2SO_4 solution at +10 mA (Fig. 4d). The active faceted np-Ru exhibited a stable overpotential over 6 hours, supporting the reaction stability of the developed Ru {10$\bar{1}$0} facets (see also Fig. S19† for chronoamperometric tests). TEM characterization has also confirmed that the np-Ru catalyst after the stability test retained not only the nanoporous structure but also the catalytically active {10$\bar{1}$0} facets (Fig. S20 and S21†).

Conclusions

A nanoporous ruthenium (np-Ru) catalyst surrounded by reaction-active {10$\bar{1}$0} facets has been successfully materialized *via* leaching of a lamellar Ru–CeO$_2$ nanocomposite that spontaneously emerges from a Ru$_2$Ce precursor alloy in an oxidative atmosphere. Np-Ru can be a rational alternative to Pt catalysts because of its low hydrogen evolution reaction (HER) overpotential, high H_2 generation rate, long-term reaction stability, and low material cost. The active faceted np-Ru can be further improved in catalytic performance through hybridization with promoter nanomaterials such as carbon nanotubes and/or graphene materials, contributing to future social implementation of CO$_2$-free hydrogen resources.[42,43] Finally, the proposed material design strategy for np-Ru, *i.e.*, the utilization of nanophase separation of precursor alloys, will open up unexplored synthetic routes toward a wide variety of nanoporous metals.

Conflicts of interest

There are no conflicts to declare.

Acknowledgements

Notes and references

1 S. Bhattacharyya, Y. Mastai, R. Narayan Panda, S.-H. Yeon and M. Z. Hu, *J. Nanomater.*, 2014, **2014**, 275796.

2 S. Ameen, M. S. Akhtar, R. Godbole and H.-S. Shin, *An Introduction to Nanoporous Materials*, IntechOpen, 2019.

3 R. Ron, E. Haleva and A. Salomon, *Adv. Mater.*, 2018, **30**, 1706755.

4 Y. Tang, B. Tang, Q. Li, J. Qing, L. Lu and K. Chen, *Exp. Therm. Fluid Sci.*, 2013, **44**, 194–198.

5 Q. Xu, H. Wang, X. Jiang and Y. Yamauchi, in *Nanoporous Materials*, CRC Press, 2013, pp. 183–200.

6 B. Jiang, C. Li, Ö. Dag, H. Abe, T. Takei, T. Imai, M. S. A. Hossain, M. T. Islam, K. Wood, J. Henzie and Y. Yamauchi, *Nat. Commun.*, 2017, **8**, 1–8.

7 B. R. Wiesenauer and D. L. Gin, *Polym. J.*, 2012, **44**, 461–468.

8 X. Zhang, W. Lu, J. Dai, L. Bourgeois, J. Yao, H. Wang, J. R. Friend, D. Zhao and D. R. MacFarlane, *Sci. Rep.*, 2014, **4**, 1–5.

9 H. Luo, L. Sun, Y. Lu and Y. Yan, *Langmuir*, 2004, **20**, 10218–10222.

10 J. H. Nam, Y. Y. Jang, Y. U. Kwon and J. Do Nam, *Electrochem. Commun.*, 2004, **6**, 737–741.

11 V. Malgras, Q. Ji, Y. Kamachi, T. Mori, F.-K. Shieh, K. C.-W. Wu, K. Ariga and Y. Yamauchi, *Bull. Chem. Soc. Jpn.*, 2015, **88**, 1171–1200.

12 L. Zhang, H. Chang, A. Hirata, H. Wu, Q. K. Xue and M. Chen, *ACS Nano*, 2013, **7**, 4595–4600.

13 P. Haldar and A. Chatterjee, *Acta Mater.*, 2017, **127**, 379–388.

14 L. Zeng, C. You, X. Cai, C. Wang, X. Zhang and T. Liang, *J. Mater. Res. Technol.*, 2020, **9**, 6909–6915.

15 C. Qin, M. Zhang, B. Li, Y. Li and Z. Wang, *Mater. Lett.*, 2020, **258**, 126823.

16 Q. Lu, G. S. Hutchings, W. Yu, Y. Zhou, R. V. Forest, R. Tao, J. Rosen, B. T. Yonemoto, Z. Cao, H. Zheng, J. Q. Xiao, F. Jiao and J. G. Chen, *Nat. Commun.*, 2015, **6**, 1–8.

17 Y. T. Kim, P. P. Lopes, S. A. Park, A. Y. Lee, J. Lim, H. Lee, S. Back, Y. Jung, N. Danilovic, V. Stamenkovic, J. Erlebacher, J. Snyder and N. M. Markovic, *Nat. Commun.*, 2017, **8**, 1–8.

18 J. Erlebacher and I. McCue, *Acta Mater.*, 2012, **60**, 6164–6174.

19 S. Yang, Y. J. Tak, J. Kim, A. Soon and H. Lee, *ACS Catal.*, 2017, **7**, 1301–1307.

20 P. Xie, T. Pu, A. Nie, S. Hwang, S. C. Purdy, W. Yu, D. Su, J. T. Miller and C. Wang, *ACS Catal.*, 2018, **8**, 4044–4048.

21 X. Chen, X. Chen, S. Cai, J. Chen, W. Xu, H. Jia and J. Chen, *Chem. Eng. J.*, 2018, **334**, 768–779.

This journal is © The Royal Society of Chemistry 2020

J. Mater. Chem. A, 2020, **8**, 19788–19792 | 19791

22 G. Arteaga, L. M. Rivera-Gavidia, S. J. Martínez, R. Rizo, E. Pastor and G. García, *Surfaces*, 2019, **2**, 16–31.

23 G. Zhao, K. Rui, S. X. Dou and W. Sun, *Adv. Funct. Mater.*, 2018, **28**, 1803291.

24 M. Hakamada, J. Motomura, F. Hirashima and M. Mabuchi, *Mater. Trans.*, 2012, **53**, 524–530.

25 Q. Zhou, H. Yang and C. Xu, *Int. J. Hydrogen Energy*, 2016, **41**, 12714–12721.

26 S. Drouet, J. Creus, V. Collière, C. Amiens, J. García-Antón, X. Sala and K. Philippot, *Chem. Commun.*, 2017, **53**, 11713–11716.

27 Y. Li, L. A. Zhang, Y. Qin, F. Chu, Y. Kong, Y. Tao, Y. Li, Y. Bu, D. Ding and M. Liu, *ACS Catal.*, 2018, **8**, 5714–5720.

28 A. S. B. M. Najib, X. Peng, A. Hashimoto, T. Shoji, T. Iida, Y. Bai and H. Abe, *Chem.–Asian J.*, 2019, **14**, 201900542.

29 S. Gates-Rector and T. Blanton, *Powder Diffr.*, 2019, **34**, 352–360.

30 N. S. Marinkovic, M. B. Vukmirovic and R. R. Adzic, in *Modern Aspects of Electrochemistry*, Springer, New York, 2008, pp. 1–52.

31 M. G. Walter, E. L. Warren, J. R. McKone, S. W. Boettcher, Q. Mi, E. A. Santori and N. S. Lewis, *Chem. Rev.*, 2010, **110**, 6446–6473.

32 Y. Gorlin and T. F. Jaramillo, *J. Am. Chem. Soc.*, 2010, **132**, 13612–13614.

33 M. B. Zakaria, *RSC Adv.*, 2016, **6**, 10341–10351.

34 M. B. Zakaria, M. Hu, M. Pramanik, C. Li, J. Tang, A. Aldalbahi, S. M. Alshehri, V. Malgras and Y. Yamauchi, *Chem.–Asian J.*, 2015, **10**, 1541–1545.

35 A. A. Alireza, N. Hamnabard, S. M. H. Meshkati, M. Pakan and Y. H. Ahn, *Dalton Trans.*, 2019, **48**, 5429–5443.

36 Z. Zhou, L. Wei, Y. Wang, H. E. Karahan, Z. Chen, Y. Lei, X. Chen, S. Zhai, X. Liao and Y. Chen, *J. Mater. Chem. A*, 2017, **5**, 20390–20397.

37 C. C. L. McCrory, S. Jung, I. M. Ferrer, S. M. Chatman, J. C. Peters and T. F. Jaramillo, *J. Am. Chem. Soc.*, 2015, **137**, 4347–4357.

38 B. Seo, D. S. Baek, Y. J. Sa and S. H. Joo, *CrystEngComm*, 2016, **18**, 6083–6089.

39 L. X. Chen, Z. W. Chen, Y. Wang, C. C. Yang and Q. Jiang, *ACS Catal.*, 2018, **8**, 8107–8114.

40 A. Kahyarian, B. Brown and S. Nesic, *J. Electrochem. Soc.*, 2017, **164**, H365–H374.

41 T. Shinagawa, A. T. Garcia-Esparza and K. Takanabe, *Sci. Rep.*, 2015, **5**, 1–21.

42 Y. Zheng, Y. Jiao, Y. Zhu, L. H. Li, Y. Han, Y. Chen, M. Jaroniec and S. Z. Qiao, *J. Am. Chem. Soc.*, 2016, **138**, 16174–16181.

43 D. H. Kweon, M. S. Okyay, S.-J. Kim, J.-P. Jeon, H.-J. Noh, N. Park, J. Mahmood and J.-B. Baek, *Nat. Commun.*, 2020, **11**, 1278.

19792 | *J. Mater. Chem. A*, 2020, **8**, 19788–19792

This journal is © The Royal Society of Chemistry 2020